

Mass-Conserving Inversion of NO_x Emissions and Inferred Combustion Technologies in Energy Rich Northern China Based on Multi-Year Daily Remotely Sensed and Continuous Surface Measurements

Xiaolu Li¹, Jason Blake Cohen², Kai Qin³, Hong Geng⁴, Liling Wu⁵, Xiaohui Wu⁶, Chengli Yang⁶, Rui Zhang⁷, and Liqin Zhang⁸

¹Institute of Environmental Science

²School of Environment Science and Spatial Informatics, China University of Mining and Technology

³China University of Mining and Technology

⁴Shanxi University

⁵School of Environment, Tsinghua University

⁶Shanxi Dadi Ecology and Environment Technology Research Institute

⁷Consulting Service Center of Ecologic and Environmental Protection of Shanxi Province (Shanxi Academy for Environment Planning)

⁸Monitoring and Emergency Response Center of Ecology and Environment of Shanxi Province (Shanxi Institute of Ecologic and Environmental Science)

November 22, 2022

Abstract

Nitrogen oxides (NO_x) are markers of combustion contributing to ozone, secondary aerosol, and acid rain, and are required to run models focusing on atmospheric environmental protection. This work presents a new model free inversion estimation framework using daily TROPOMI NO₂ columns and observed fluxes from the continuous emissions monitoring systems (CEMS) to quantify emissions of NO_x at 0.05°×0.05°. The average emission is 0.72±0.11Tg/yr from 2019 through 2021 over Shanxi, a major energy producing and consuming province in Northern China. The resulting emissions demonstrates significant spatial and temporal differences with bottom-up emissions databases, with 54% of the emissions concentrated in 25% of the total area. Two major forcing factors are horizontal advective transport (352.0±51.2km) and first order chemical loss (13.1±1.1hours), consistent with a non-insignificant amount of NO_x advected into the free troposphere. The third forcing factor, the computed ratio of NO_x/NO₂, on a pixel-by-pixel basis has a significant correlation with the combustion temperature and energy efficiency of large energy consuming sources. Specifically, thermal power plants, cement, and iron and steel companies have high NO_x/NO₂ ratios, while coking, industrial boilers, and aluminum show low ratios. Variance maximization applied to the daily TROPOMI NO₂ columns identifies three modes dominate the variance and attributes them to this work's computed emissions, remotely sensed TROPOMI UVAI, and transport based on TROPOMI CO. Using satellite observations for emission estimates in connection with CEMS allows the rapid update of emissions, while also providing scientific support for the identification and attribution of anthropogenic sources.

1 **Mass-Conserving Inversion of NO_x Emissions and Inferred Combustion**
2 **Technologies in Energy Rich Northern China Based on Multi-Year Daily Remotely**
3 **Sensed and Continuous Surface Measurements**
4

5 **Xiaolu Li^{1,2}, Jason Blake Cohen^{2*}, Kai Qin^{2*}, Hong Geng¹, Liling Wu³, Xiaohui Wu⁴,**
6 **Chengli Yang⁴, Rui Zhang⁵, Liqin Zhang⁶**

7 ¹Institute of Environmental Science, Shanxi University, Taiyuan, China

8 ²School of Environment and Spatial Informatics, China University of Mining and Technology,
9 Xuzhou, China

10 ³School of Environment, Tsinghua University, Beijing, China

11 ⁴Shanxi Dadi Ecology and Environment Technology Research Institute Co., Ltd., Taiyuan, China

12 ⁵Shanxi Institute of Eco-environmental Planning and Technology, Taiyuan, China

13 ⁶Monitoring and Emergency Response Center of Ecology and Environment of Shanxi Province
14 (Shanxi Institute of Ecologic and Environmental Science), Taiyuan, China

15
16 Corresponding authors: J. B. Cohen (jasonbc@alum.mit.edu), K. Qin (qinkai@cumt.edu.cn)
17

18 **Key Points:**

- 19 • Daily-scale, grid-by-grid emissions calculated using TROPOMI NO₂ and CEMS compare
20 well with known spatial and temporal features
- 21 • Identification and quantification of different energy consuming combustion technologies
22 based on the method's constrained NO_x/NO₂ ratio
- 23 • Variance maximization on TROPOMI NO₂ identifies and attributes variation to NO_x
24 emissions, UVAI, and atmospheric transport of CO
25

26 **Abstract**

27 Nitrogen oxides (NO_x) are markers of combustion contributing to ozone, secondary aerosol, and
28 acid rain, and are required to run models focusing on atmospheric environmental protection. This
29 work presents a new model free inversion estimation framework using daily TROPOMI NO_2
30 columns and observed fluxes from the continuous emissions monitoring systems (CEMS) to
31 quantify emissions of NO_x at $0.05^\circ \times 0.05^\circ$. The average emission is $0.72 \pm 0.11 \text{ Tg/yr}$ from 2019
32 through 2021 over Shanxi, a major energy producing and consuming province in Northern
33 China. The resulting emissions demonstrates significant spatial and temporal differences with
34 bottom-up emissions databases, with 54% of the emissions concentrated in 25% of the total area.
35 Two major forcing factors are horizontal advective transport ($352.0 \pm 51.2 \text{ km}$) and first order
36 chemical loss ($13.1 \pm 1.1 \text{ hours}$), consistent with a non-insignificant amount of NO_x advected into
37 the free troposphere. The third forcing factor, the computed ratio of NO_x/NO_2 , on a pixel-by-
38 pixel basis has a significant correlation with the combustion temperature and energy efficiency
39 of large energy consuming sources. Specifically, thermal power plants, cement, and iron and
40 steel companies have high NO_x/NO_2 ratios, while coking, industrial boilers, and aluminum show
41 low ratios. Variance maximization applied to the daily TROPOMI NO_2 columns identifies three
42 modes dominate the variance and attributes them to this work's computed emissions, remotely
43 sensed TROPOMI UVAI, and transport based on TROPOMI CO. Using satellite observations
44 for emission estimates in connection with CEMS allows the rapid update of emissions, while
45 also providing scientific support for the identification and attribution of anthropogenic sources.

46 **Plain Language Summary**

47 Daily remotely sensed measurements of NO_2 from satellite and ground-based measurements of
48 NO_x fluxes from industrial sources, in combination with a simplified mathematical method are
49 used to estimate the emissions of NO_x . Sources are identified in regions previously not
50 identified and quantified in regions which have been mis-identified or otherwise are missing up-
51 to-date inventories. The underlying driving terms of this approach allow for flexible estimation
52 of three driving factors: the thermodynamics of combustion and rapid atmospheric adjustment,
53 first order chemical loss, and atmospheric transport. A deeper analysis with the thermodynamic
54 term matches with different large energy consuming sources, being able to separate very hot
55 sources such as power generation, iron, and cement from cooler or less energy efficient sources
56 such as coking, industrial boilers, and aluminum smelting. The second and third terms are
57 consistent with chemical and dynamical theory, and indicate that some of the emissions are
58 lofted high above the surface. Analysis of the variance in the NO_2 columns identifies three major
59 factors contributing to extremes: this work's emissions, measured UV radiation, and
60 measurements of the gradient of measured CO. While the average emissions is not considerably
61 different from existing datasets, the day-to-day and geospatial differences are significant.

62 **1 Introduction**

63 Economic growth has always been accompanied by air pollution, with serious
64 consequences associated with higher atmospheric loadings. To alleviate severe air quality
65 problems, the Chinese government has been implementing new air pollution controls, with the
66 aim of producing higher-quality development. Two recent examples are the Air Pollution
67 Prevention and Control Action Plan from 2013 to 2017 and the Three-Year Action Plan for
68 Winning the Battle in Defense of Blue Sky from 2018 to 2020 (Geng et al., 2019; Jiang et al.,
69 2021), which have led to a significant reduction in annual average concentrations of particulate

70 matter (PM), sulfur dioxide (SO₂) and carbon monoxide (CO) in Shanxi Province . Shanxi is
71 selected for this study, as it is a highly energy rich location that produces more than 25% of all of
72 China's coal, as well as having substantial industry that consumes a significant amount of the
73 coal for both local energy production and export, steel, cement, coke, and aluminum production,
74 among other economic activities (Li et al., 2022). Furthermore, due to its relatively dry climate,
75 high elevation, and mountainous geography, it has complex underlying natural factors also
76 impacting its atmospheric environment. For these reasons, there have also been minor increases
77 in the annual average concentration of both ozone (O₃) and nitrogen dioxide (NO₂) observed in
78 Shanxi between 2015 and 2020 (Shanxi DEE., 2016, 2021).

79 The sum of NO₂ and Nitrogen Monoxide (NO) is frequently grouped as nitrogen oxides
80 (herein termed NO_x), which is an important trace gas impacting of the Earth's atmosphere
81 because it is a strong marker of anthropogenic combustion-related pollution, a precursor to ozone
82 (Jacob et al., 1993), secondary aerosol (Beirle et al., 2011) and acid rain (Singh & Agrawal,
83 2007). In order to gain a better understanding of NO_x and its impacts, precise and quantitative
84 emissions inventories are crucial information for policy makers, air quality modelers, and anyone
85 who works with chemical transport or chemical climate models, among others (Crippa et al.,
86 2018; Hoesly et al., 2018). To improve the understanding of pollution and its environmental
87 impacts, accurate quantitative knowledge of NO_x emissions at a very high horizontal resolution
88 (e.g., 0.05°×0.05°) and daily temporal resolution is important, but tends to be either lacking
89 and/or increasingly uncertain (Kong et al., 2019; Zheng et al., 2017).

90 Presently, most emission inventories are compiled from statistics on emitting activities
91 and associated typical emission factors, herein called “Bottom Up” approaches, which are
92 subject to substantial uncertainties. On-site surveys are time consuming and resource demanding,
93 and therefore difficult to be applied to a large domain in a timely manner (Mijling & van der A,
94 2012; Zhao et al., 2011). Differences between small field studies and controlled laboratory
95 combustion experiments and real-world examples also are quite significant, with super-emitters
96 known to create large differences when using insufficiently large datasets (Zavala et al., 2006).
97 With low temporal resolution these bottom-up inventories are not able to keep up with rapid
98 changes in industries and economic activities, and therefore are not very good at tracking
99 atmospheric emissions under actual existing environmental conditions, limiting their use
100 (Mijling & van der A, 2012).

101 Attempts at top-down emissions inventories have been made by the community, with
102 most focusing on applications to long-lived gasses (CH₄, CFCs, and N₂O), since their chemical
103 decay is very slow compared with their transport processes, allowing for much simpler set of
104 equations required to perform the inversion (Chen & Prinn, 2006; Tu, Hase, et al., 2022). Only a
105 very small number of past works have focused on top-down emissions estimation of short-lived
106 species, and the few that have always do so under a set of idealized conditions. Some limit their
107 investigations to where there is a strong single point source surrounded by what is otherwise
108 relatively clean (Lin et al., 2020), others use an underlying model to approximate chemical and
109 transport properties of the short lived species over a pseudo region which is climatologically
110 similar, and others use highly complex or overfitting approaches such as data assimilation and
111 Kalman filters which work very well but are susceptible to underlying model and scientific
112 uncertainty, as well as being extremely costly to run (Cohen & Wang, 2014; Zhang et al.,
113 2021; Hu et al., 2022). Others have attempted to use satellite observations to scale existing top-
114 down emissions inventories, to make spatially consistent, high spatial resolution maps, but have

115 a hard time being applied in regions where the a priori emission is zero (Liu & Cohen, 2022;
116 Wang et al., 2021).

117 This study takes advantage of the respective strengths of top-down and bottom-up
118 emissions estimation by applying a new, fast, first-order approach based on daily measurements
119 of remotely sensed NO₂ from the Tropospheric Monitoring Instrument (TROPOMI), winds, and
120 mass conserving estimates of in-situ chemical and physical processing to estimate the daily NO_x
121 emissions on a mesoscale grid at (0.05°×0.05°) from 2019 through 2021. This work relies on the
122 continuous emissions monitoring systems (CEMS) measurements from significant combustion
123 sources as the source of a priori emission information. This net combination of factors does not
124 rely on complex models, and allows a flexible approximation of the first order driving forces of
125 thermodynamics, chemistry, and transport. This unique perspective is capable of inverting
126 emissions using different driving forces under different but realistic environmental conditions,
127 including during different months of the year, over multi-year changes in the environment, under
128 high UV and low UV conditions, under complex meteorological domains, and over sources
129 which are both thermodynamically stable as well as unstable. Finally, this approach allows a
130 robust error quantification, and compares very well with the measured spatial and temporal
131 variation in the underlying remotely sensed NO₂ columns.

132 **2 Materials and Methods**

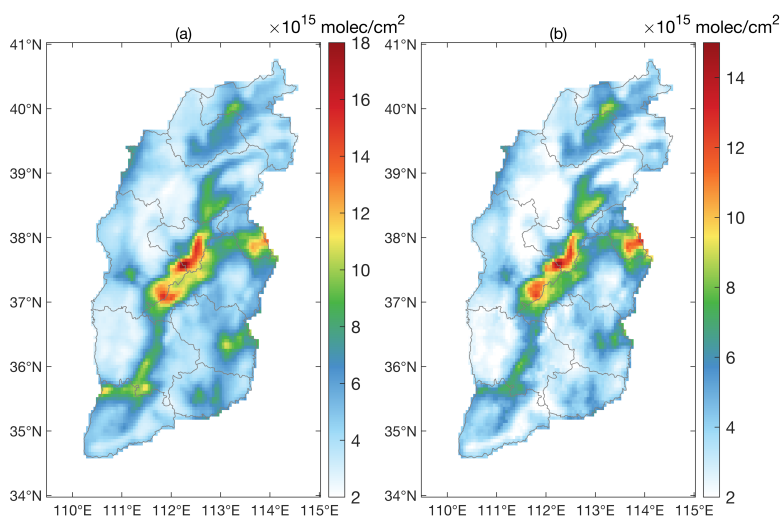
133 2.1 Tropospheric Vertical Column Measurements from TROPOMI

134 TROPOMI measures reflected solar radiation in the UV, visible, and Near IR bands
135 following a sun-synchronous, low-earth orbit with an equator overpass time of approximately
136 13:30 local solar time, allowing daily-scale measurements across the globe (Goldberg et al.,
137 2019; Tu, Schneider, et al., 2022; Veefkind et al., 2012). Starting from August 2019, the spatial
138 resolution of TROPOMI has been refined to 5.5km×3.5km (Lange et al., 2022). This study
139 specifically uses three distinct products measured by TROPOMI over different radiative bands,
140 but at the same place and time: NO₂, CO, and UVAI.

141 This work specifically uses daily level-2 version 2.3.1 tropospheric NO₂ columns, daily
142 level-2 version 2.2.0 CO columns, and daily level-2 version 2.2.0 UVAI over Shanxi Province.
143 All available days and swaths corresponding to the time period from 1 January 2019 through 14
144 November 2021 are analyzed (<https://disc.gsfc.nasa.gov/datasets>). Overlapping NO₂, CO, and
145 UVAI column pixels in each swath are resampled to a common latitude-longitude grid at
146 0.05°×0.05° using weighted polygons (<http://stcorp.github.io/harp/doc/html/index.html>). Before
147 use, it is required that all TROPOMI data is quality assured, specifically insisting that each pixel
148 has a “qa_value” greater than 0.75, that the “cloud radiance fraction” is smaller than 0.5, and that
149 scenes covered by snow/ice, errors and similar problematic retrievals are removed (Eskes, H.,
150 2021). Furthermore, in the case of NO₂, an additional filter is applied to avoid issues where the
151 signal is possibly smaller than the uncertainty range of $1.0 \times 10^{15} + 30\%$ molec/cm² (Qin et al.,
152 2022), leading to all grids with a column loading smaller than 1.4×10^{15} molec/cm² being
153 discarded. This combination of assumptions ensures that the data used should be of higher
154 precision than the a priori emissions datasets used later in this work.

155 The TROPOMI NO₂ columns used in this study can portray the spatial and temporal
156 distribution of sources in a high amount of detail, including being able to effectively identify
157 spatial hotspots (Griffin et al., 2019). The climatological mean and standard deviation of these

158 columns are shown in Figure 1, and are consistent with surface measurements indicating that the
 159 most polluted areas with respect to NO₂ in Shanxi are mainly concentrated in Fen River valley
 160 bottom area, containing Taiyuan Basin, Xinding Basin, Linfen Basin, and Yangquan City. Areas
 161 with a high standard deviation and relatively low mean value are observed in regions where new
 162 economic development zones containing power plants, coke enterprises and some other raw
 163 materials producing factories have been established, as observed in Datong. Areas with a
 164 relatively high standard deviation and relatively high mean value are indicative of high
 165 urbanization, and correspond consistently with the Taiyuan Basin, Xinding Basin, and southern
 166 Yangquan. Areas with a high average value and a low standard deviation correspond with areas
 167 which have a fewer number of temporally consistent emissions sources, as is observed in some
 168 high altitude areas, and small parts of the Linfen Basin, central Changzhi, Lvliang and Jincheng.



169
 170 **Figure 1.** Climatology of TROPOMI daily NO₂ column loadings from 2019 through 2021: (a)
 171 mean, and (b) standard deviation.

172 2.2 A Prior Emissions inventories

173 2.2.1 CEMS

174 CEMS was introduced by the Ministry of Environmental Protection of China in 2007 to
 175 monitor and manage the emissions of certain (mainly high-emitting) plants (Karplus et al., 2018;
 176 Schreifels et al., 2012). These systems make actual measurements of stack concentration PM,
 177 SO₂ and NO_x, as discharged from coal power plants, steel and iron plants, aluminum smelters,
 178 coke plants, coal-fired boilers and others, all in real-time (Tang et al., 2020; Zhang & Schreifels,
 179 2011). Statistics of the emissions sites monitored in Shanxi are given in Table 1 and displayed in
 180 Figure 2. The NO_x concentration was measured in two different ways: one converts NO₂ to NO
 181 and measures the NO concentration uniformly, the other measures both NO₂ and NO, and
 182 converts the total amount into an NO₂ mass concentration. Unfortunately, the results are not
 183 labeled as to which device was used at each individual stack, and therefore some error is
 184 introduced.

185 In this work, all available CEMS monitors of daily-scale emissions from 2019 to 2021
 186 were obtained from the Department of Ecology and Environment of Shanxi Province (original
 187 data from the government repository located at <https://sthjt.shanxi.gov.cn/wryjg/>, and available
 188 in English at <https://figshare.com/s/22782c33cbc4e61afd25>), with the government making great
 189 effort to regulate the CEMS network and to ensure the reliability of CEMS data (Tang et al.,
 190 2020). Before using the data, preprocessing includes using google earth to correct the location of
 191 the factories, removing all null observations, and setting abnormal values (including zero or
 192 negative fluxes, and abnormally large fluxes) to NaN. The overall percentage of abnormal values
 193 is found to account for 0.14%, 0.09%, and 0.18% of the raw data respectively for 2019, 2020 and
 194 2021. The formula used to calculate NO_x emissions is given in equation (1)

$$195 \quad E_d = \overline{C}_h \times \overline{Q}_h \times 24 \quad (1)$$

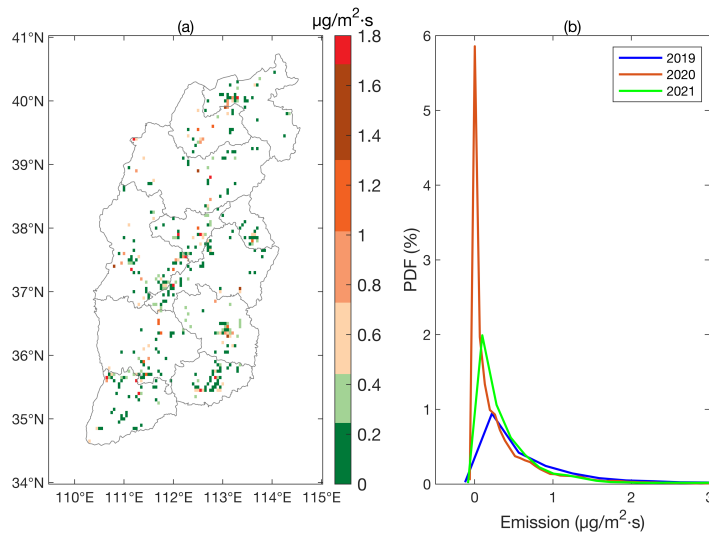
196 where \overline{C}_h is the daily average of hourly NO_x concentration and \overline{Q}_h is the daily average of hourly
 197 wet flue gas flow under actual working conditions following procedure HJ76-2017 (Zhang &
 198 Schreifels, 2011). The uncertainty of NO_x concentration (C_h) when $C_h \geq 513 \text{ mg/m}^3$ is 85%, when
 199 $103 \text{ mg/m}^3 \leq C_h < 513 \text{ mg/m}^3$ is $\pm 41 \text{ mg/m}^3$, when $41 \text{ mg/m}^3 \leq C_h < 103 \text{ mg/m}^3$ is $\pm 30\%$, and when
 200 $C_h < 41 \text{ mg/m}^3$ is $\pm 12 \text{ mg/m}^3$. After quality control, the emission intensity on a grid-by-grid basis is
 201 found to be $0.54 \pm 0.40 \mu\text{g/m}^2 \cdot \text{s}$, $0.34 \pm 0.26 \mu\text{g/m}^2 \cdot \text{s}$, and $0.39 \pm 0.24 \mu\text{g/m}^2 \cdot \text{s}$ for 2019, 2020 and
 202 2021, respectively. Grid-by-grid 3-year climatological emissions, and PDFs of annual grid-by-
 203 grid average emissions are given in Figure 2.

204 **Table 1.** Summary statistics for plants included in CEMS.

Year	Number of Companies	Number of Stacks monitored	Missing days (d)	Percentage of missing days (%)
2019	470	1557	102	27.9
2020	542	2187	24	6.6
2021	513	1806	0	0

205

206



207

208 **Figure 2:** Climatology of daily CEMS emissions data from 2019 through 2021: (a) 3-year
 209 average gridded NO_x Emissions, and (b) PDFs of day-by-day and grid-by-grid Emissions over
 210 individual years.

211

2.2.2 Multi-resolution Emission Inventory for China (MEIC)

212

213

214

215

216

217

218

219

220

221

222

223

224

225

MEIC provides 0.25°×0.25° bottom-up emissions of anthropogenic air pollutants over mainland China, with monthly NO_x emissions provided for the agriculture, industry, power, residential and transportation sectors. This work uses data from 2019 and 2020 (Zheng et al., 2021). To match with the higher resolution TROPOMI grids, the MEIC data is mapped to the TROPOMI 0.05°×0.05° grid, with each grid assigned the same flux as the underlying MEIC grid. To ensure quality control, given that many very low values may fall within the uncertainty of the bottom-up emissions process (Bond, 2004; J. B. Cohen & Wang, 2014; Crippa et al., 2018) different minimum cutoffs have been applied to the MEIC data prior to use as an a priori, which herein are labeled as MEIC014 (discarding all values smaller than 0.14 µg/m²·s) and MEIC050 (discarding all values smaller than 0.50 µg/m²·s). MEIC014 discards 69% and 71% percent of the grids respectively in 2019 and 2020, while MEIC050 discards 91% and 92% grids respectively. The mean daily values and PDFs of the grid-by-grid climatological mean data over Shanxi Province from 2019 January 1 to 2020 December 31 are given in Figure 3(a) and Figure 3 (b).

226

2.2.3 Merged MEIC and CEMS Emissions

227

228

229

230

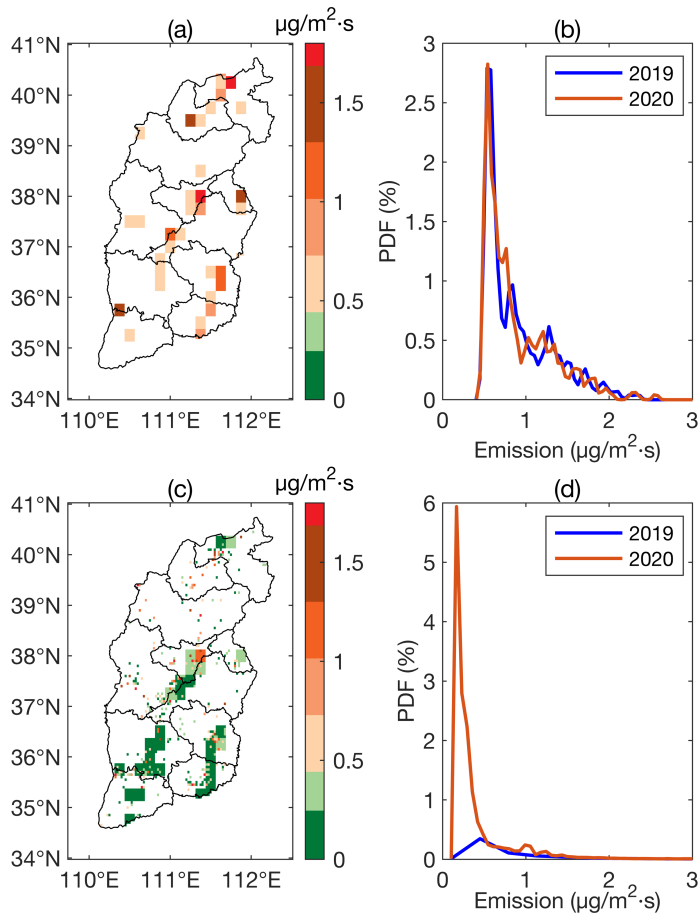
231

232

233

The already processed CEMS and MEIC emissions which occur on the same grid at the same time are fused into a new joint product. This new product [hereafter called Merged Emissions] contains MEIC with power plant and industrial emissions removed, summed together with the CEMS data. This is done on a day-to-day basis from January 2019 through December 2020. Since there are many very small values in the merged inventory which are not realistic, all grids with data lower than 0.14 µg/m²·s, 91% and 92% of grids respectively in 2019 and 2020, are excluded in a second merged product [hereafter called Merged014]. The climatological mean

234 of daily emissions, and histograms of day-by-day and grid-by-grid values over Shanxi are given
 235 in Figure 3(c) and Figure 3 (d).



236

237 **Figure 3:** Daily average MEIC and Merged emissions from 2019 to 2020: (a) Climatological
 238 mean of MEIC050; (b) histograms of day-by-day and grid-by-grid MEIC050 over individual
 239 years; (c) Climatological mean of Merged014; (d) histograms of day-by-day and grid-by-grid
 240 Merged014 over individual years.

241 2.3 Wind

242 Wind speed and direction are from the European Centre for Medium-Range Weather
 243 Forecasts, ERA-5 reanalysis product. In specific, we use 6-hourly 6AM UTC u and v wind
 244 products (closest in terms of time to the TROPOMI overpass) at 900mb and $0.25^\circ \times 0.25^\circ$
 245 resolution (Lange et al., 2022), available at [https://www.ecmwf.int/en/forecasts/dataset/ecmwf-](https://www.ecmwf.int/en/forecasts/dataset/ecmwf-reanalysis-v5)
 246 [reanalysis-v5](https://www.ecmwf.int/en/forecasts/dataset/ecmwf-reanalysis-v5). To merge the wind data in space and time with the TROPOMI observations, they
 247 are linearly interpolated to the center of each TROPOMI $0.05^\circ \times 0.05^\circ$ grid (Fioletov et al., 2022).
 248 The reason for choosing the 900mb level is two-fold. First, Shanxi has complex topography,
 249 leading to a significant amount of pollutant transport from near the ground to the lower free
 250 troposphere. Second, due to the relatively dry conditions, vertical plume-based rise is thought to
 251 not be insignificant (Wang et al., 2020). Overall, this height is a reasonable approximation of the

252 corresponding median height of the expected total NO_x emissions and median of the wind speed
253 and directions (Lange et al., 2022).

254 2.4 Variance Maximization

255 To extract the spatial and temporal features of the extremes of the remotely sensed NO₂
256 fields in an unbiased manner, the empirical orthogonal functions method is applied. This
257 technique decomposes the data into a set of orthogonal standing signals in space [EOF] and in
258 time, with those signals contributing the most to the overall variance of the underlying dataset,
259 representing unique phenomenon that control the overall characteristics of the NO₂ columns (Lin
260 et al., 2020; Zhou et al., 2016). Further details including mathematical derivations are given in
261 (Björnsson & Venegas, 1997) and (Cohen, 2014). This work retains the first three EOFs, which
262 are found to contribute to 29.7%, 8.5%, and 4.2% of the total variation, with the subsequent
263 EOFs each contributing an insignificant amount and therefore no longer considered in this work.

264 2.5 Model Free Inversion Estimation Framework

265 In the case where there is an observed change in the stock of NO_x in the atmosphere,
266 herein represented as S, this can only be accomplished by introducing some sources or sinks. The
267 first is the amount of NO_x emitted, herein represented as E, which always will increase the
268 existing stock. The second is chemical loss of NO_x, which will always lead to a decrease in the
269 existing stock. The third is the sum of pressure induced and advective transport, which may
270 either increase or decrease the stock. The chemical sinks of NO_x are dominated by the reaction
271 between NO₂ with OH (Beirle et al., 2019; Valin et al., 2013), which can be described as C. The
272 transport is herein described as D, and is calculated by the gradient of the multiple of the u and v
273 wind fields times the top-down NO_x column loadings, herein described as V_{NO_x}, which consists
274 of an advective portion (H. Wang et al., 2014) and a pressure-based portion (Mahowald et al.,
275 2005). Hence, a simple mass conservation equation for NO_x loading can be calculated as

$$276 \quad dS = E - C + D \quad (2)$$

277 Solving equation 2 for emissions on a grid-by-grid basis requires knowledge of the mass
278 change of the loading in time, and detailed consideration of chemical loss and transformation,
279 deposition, and transport. An explicit formulation of these processes into a readily solvable mass
280 balance method is derived as equation 3. However, due to the fact that TROPOMI only measures
281 NO₂ and not NO_x, a transformation is required to transform NO₂ columns into NO_x ($NO_x = \alpha_1 \cdot$
282 NO_2). These details allow transformation of the mass balance equation into equation 4, where

$$283 \quad E_{NO_x} = \frac{dV_{NO_x}}{dt} + \alpha \cdot V_{NO_x} + \alpha' \cdot \nabla(\bar{u} \cdot V_{NO_x}) \quad (3)$$

$$284 \quad E_{NO_x} = \alpha_1 \cdot \frac{dV_{NO_2}}{dt} + \alpha_1 \alpha_2 \cdot V_{NO_2} + \alpha_1 \alpha_3 \cdot (\nabla(u \cdot V_{NO_2}) + \nabla(v \cdot V_{NO_2})) \quad (4)$$

285 α_2, α_3 are the parameters related to NO_x lifetime and transport distance, respectively.

286 2.6 Additional Analytical Methods

287 This work employs multiple linear regression to fit the values of $\alpha_1, \alpha_2,$ and α_3 on a
288 month-by-month, grid-by-grid basis using all available daily measurements and equation 4.
289 Bootstrapping is a means to create a new sample to represent the parent sample distribution
290 through multiple repetitions of sampling (Liu & Cohen, 2022). In specific, the distributions of $\alpha_1,$

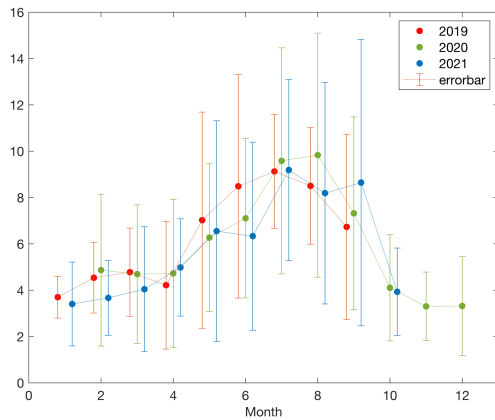
291 α_2 , and α_3 are sampled across the central 90% of their probability distributions, to use to
292 generate a set of pseudo α_1 , α_2 , and α_3 on individual grids where there is no existing a priori and
293 therefore no actual solution of these variables. These bootstrapped pseudo α_1 , α_2 , and α_3 are
294 then used on these specific grids to approximate the emissions of NO_x using equation 4 on a
295 daily basis where TROPOMI NO₂ column data and wind data is available.

296 **3 Results and Discussion**

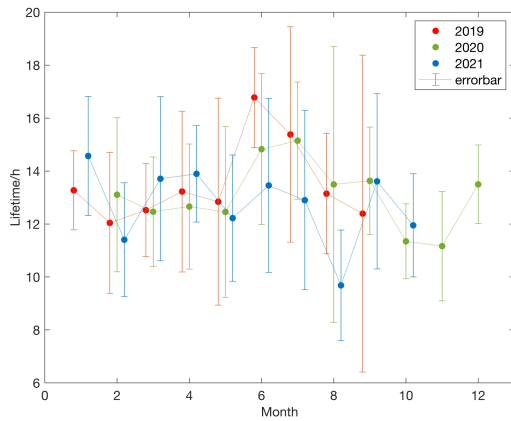
297 **3.1 Computed Emissions and Fitting Parameters Using CEMS**

298 First, the CEMS a priori emissions dataset is used together with TROPOMI NO₂ column
299 loadings, wind, and equation 4 to fit the values of α_1 , α_2 , and α_3 , as given in section 2.6. The
300 fitted coefficients are computed month-by-month over the three years of data. Their overall
301 climatological mean and standard deviation are found to be $\alpha_1=6.1\pm 1.3$, $\alpha_2=13.1\pm 1.1$ h, and
302 $\alpha_3=352.0\pm 51.2$ km. However, it is observed in the fits that there is some variability which is not
303 uniform in space and time, with the month-by-month values and standard deviations given in
304 Figure 4. In general, α_1 tends to be slightly higher during the hotter months of the year, but it
305 also has a higher variability when the UV values are high as well, making July and August the
306 only months in which it statistically has fewer small values than the other times of the year. In
307 general, α_2 tends to be quite variable, without any significant seasonal or month of year pattern.
308 Instead, both inter-annual and intra-annual variations seem to drive most of the change. Given
309 that this is related to the overall average temperature and UV availability, a complex function of
310 the plume height, cloudiness, aerosol loadings, and other factors, this is not unreasonable. The
311 absolute magnitudes of α_2 and their uncertainty range are reasonable when compared with
312 vertically integrated and 24-hour integrated chemical transport model values. In general, α_3 also
313 seems to not have any significant seasonal or monthly pattern, with inter-annual and intra-annual
314 terms seeming to dominate. The values tend to be slightly larger than chemical transport models
315 account for, but are reasonable when compared with the ultra-long-range transport simulated for
316 plumes which break the boundary layer. This range, combined with the wide mountain basins in
317 Shanxi of 200km to 300km in length, seem to provide a reasonable bound on the output results.
318

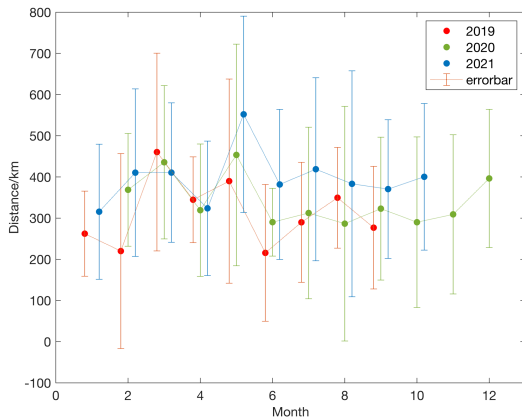
319



320



321



322

323

324

Figure 4: Monthly α_1 (top), α_2 (middle) and α_3 (bottom) calculated based on CEMS. Data from different years is provided where 2019 is in red, 2020 is in green, and 2021 is in blue.

325

326

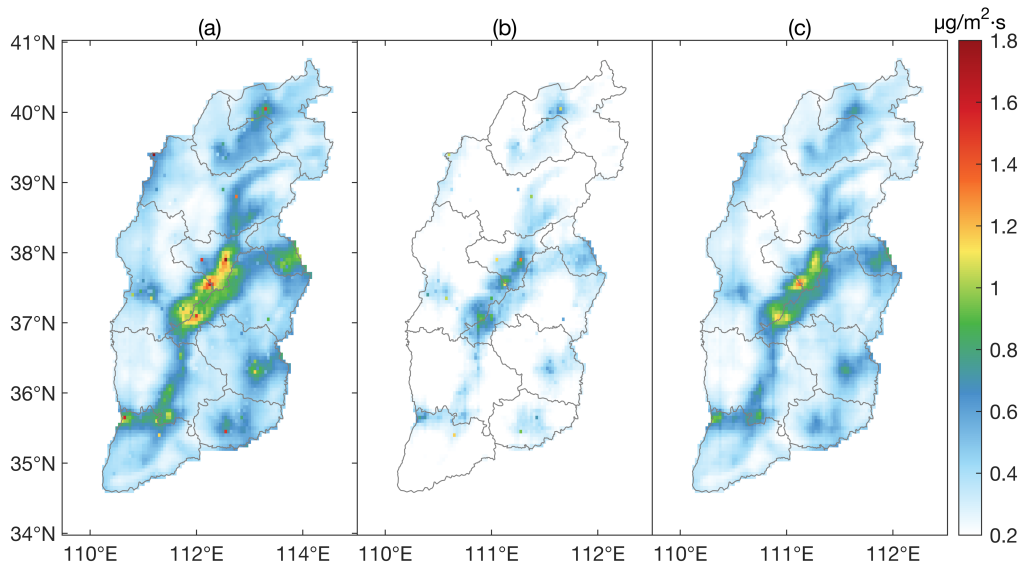
327

328

329

Next, the daily emissions of NO_x are calculated throughout the given spatial and temporal domain of interest using bootstrapping in connection with equation 4 and the fitted values of α_1 , α_2 , and α_3 . The use of the Model Free Inversion Estimation Framework [MFIEF] can effectively optimize the distribution of the inventory and perform inventory correction based on satellite

330 data, while complementing many areas where there is no existing emissions data, incomplete
 331 data, mis-characterized data, or data which may be reasonable on average but not account for
 332 daily-scale variability. The day-to-day, grid-by-grid emissions are displayed in terms of
 333 climatology, day-to-day variability, and average mean error based on the standard deviation of
 334 the bootstrap, in Figure 5. For all subsequent emissions values displayed, the numbers
 335 correspond to the sum over the daily mean \pm daily variation. It is observed that the grids with the
 336 highest NO_x emission in Shanxi are mainly concentrated in the lower Fen River valley,
 337 containing the Taiyuan Basin, the Xinding Basin, and the LinFen Basin, which also corresponds
 338 to the area containing the highest population density in the region studied. This area in total
 339 accounts for 25% of the total area of the province and contributes 54% ($0.39 \pm 0.059 \text{ Tg NO}_x/\text{yr}$)
 340 of the total ($0.72 \pm 0.11 \text{ Tg NO}_x/\text{yr}$) in Shanxi. It is of significance to note that regions with a grid-
 341 by-grid moderate amount of emissions, ranging from 0.5 to $1.5 \mu\text{g}/\text{m}^2 \cdot \text{s}$, contribute a of 38% of
 342 the emissions ($0.36 \pm 0.13 \text{ Tg NO}_x/\text{yr}$).



343

344 **Figure 5:** Daily emissions based on CEMS from Jan 2019 to Oct 2020 over Shanxi Province at
 345 $0.05^\circ \times 0.05^\circ$: (a) Climatological mean of NO_x emissions. (b) Climatological standard deviation
 346 of NO_x emissions (day-to-day variability). (c) Bootstrapping standard deviation (uncertainty).

347 3.2 Underlying Factors Contributing to Variance Maximized TROPOMI NO_2 Columns

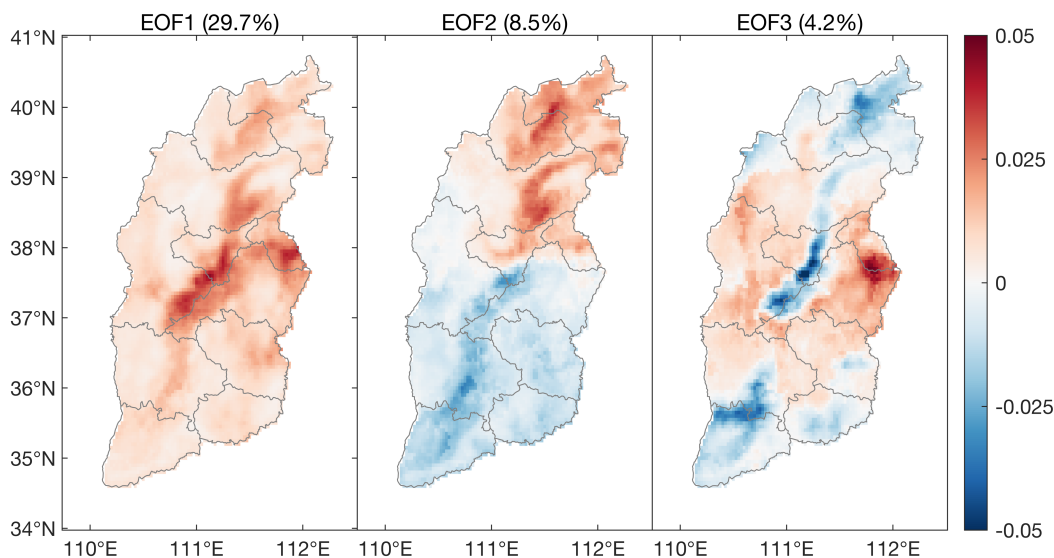
348 A deeper analysis of the factors contributing to the variance in the TROPOMI NO_2
 349 column measurements is essential to determine if the computed emissions and underlying factors
 350 are consistent with the remotely sensed fields both in terms of grid-by-grid mean value and
 351 temporal variability. Recent best practice has devised a way to ensure this consistency through
 352 the use of an Empirical Orthogonal Functions Principal Components Analysis (Cohen, 2014;
 353 Cohen et al., 2017; Lin et al., 2020), which is applied to the daily TROPOMI NO_2 columns. The
 354 three spatial modes contributing the most variation to the observed daily TROPOMI NO_2 fields
 355 [EOF1, EOF2, and EOF3] contribute 29.7%, 8.5%, and 4.2% respectively, as shown in Figure 6.

356 It is asserted that EOF1 is directly driven by the CEMS computed NO_x emissions. The
 357 comparison of EOF1 and the emissions is shown in Figure 7. By applying 4 different

358 progressively increasing cutoffs to the domain of EOF1, it is observed that as the EOF1 domain
 359 increases in magnitude, that the 3-year mean NO_x emissions computed over the same domains
 360 also increase in magnitude. Therefore, the more extreme the EOF1 value, the higher the
 361 emissions, demonstrating that the emissions are responsible for the first mode of the maximized
 362 variance.

363 Second, it is asserted that EOF2 is related to measured UV radiation, providing
 364 measurement support of the theory in which UV radiation plays a role driving the chemical
 365 decay of NO_x. Applying 4 different cutoffs to EOF2, it is observed that as the EOF2 domain
 366 increase in magnitude, that the 3-year mean measured TROPOMI UVAI decreases, as
 367 demonstrated in Figure 8. Since UVAI scales inversely with the available surface UV radiation,
 368 therefore lower UVAI implies higher available surface UV radiation, and implicitly faster
 369 chemical decay of NO_x. This result demonstrates that surface UV radiation is responsible for the
 370 second mode of the maximized variance.

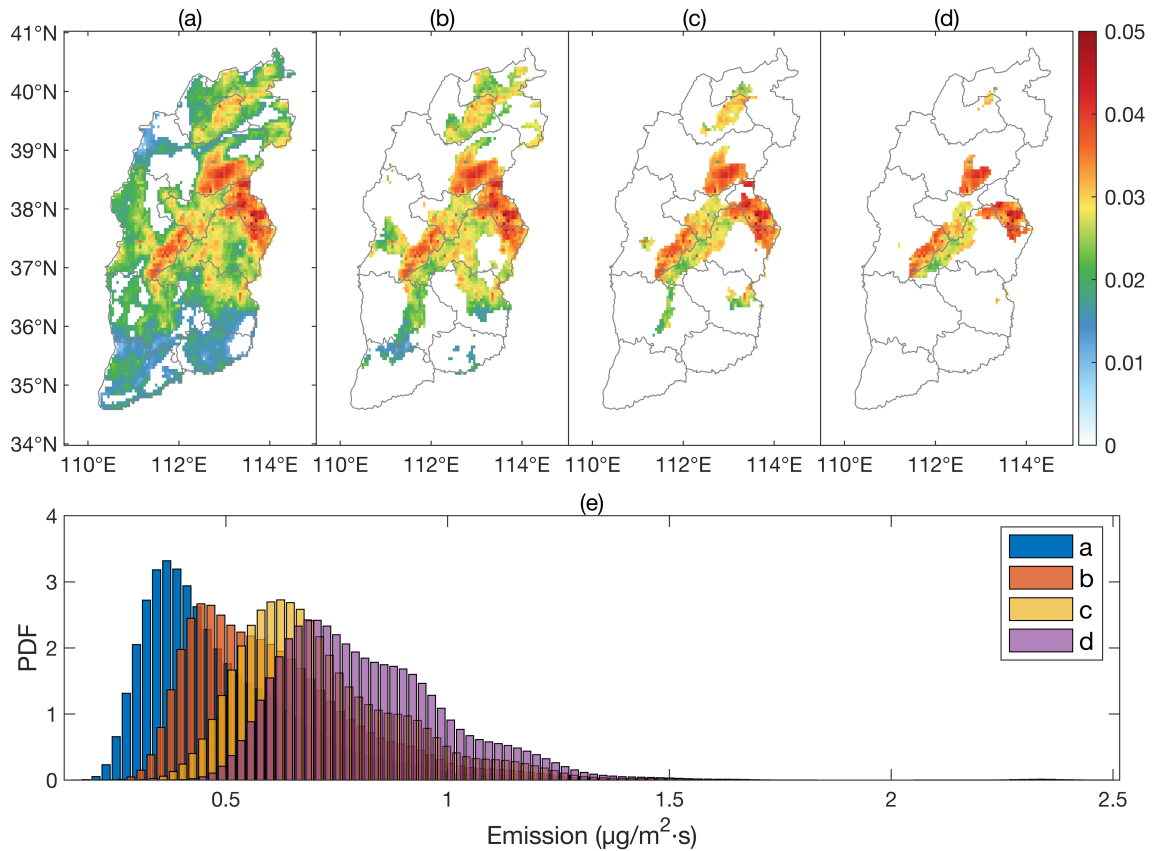
371 Finally, it is asserted that EOF3 is related to the transport of CO, which makes sense in
 372 that CO can undergo transport over longer distances than NO_x due to its slower chemical decay,
 373 and therefore represents the long-range transport of not only itself but also many other chemical
 374 species into the local environment being analyzed. This term has been specifically computed by
 375 taking the variance of the multiple of wind and TROPOMI measured CO column loadings,
 376 specifically $\nabla(\bar{u} \cdot V_{CO})$. Similarly to the above cases, it is demonstrated that as 4 different cutoffs
 377 are applied to EOF3, it is observed that as the EOF3 domain increase in magnitude, so does the
 378 measured long-range transport based on TROPOMI CO also increase, as observed in Figure 9.
 379 Therefore, long-range transport is responsible for the third mode of the maximized variance.
 380



381

382 **Figure 6:** Spatial distribution map of (a) EOF1, (b) EOF2, and (c) EOF3.

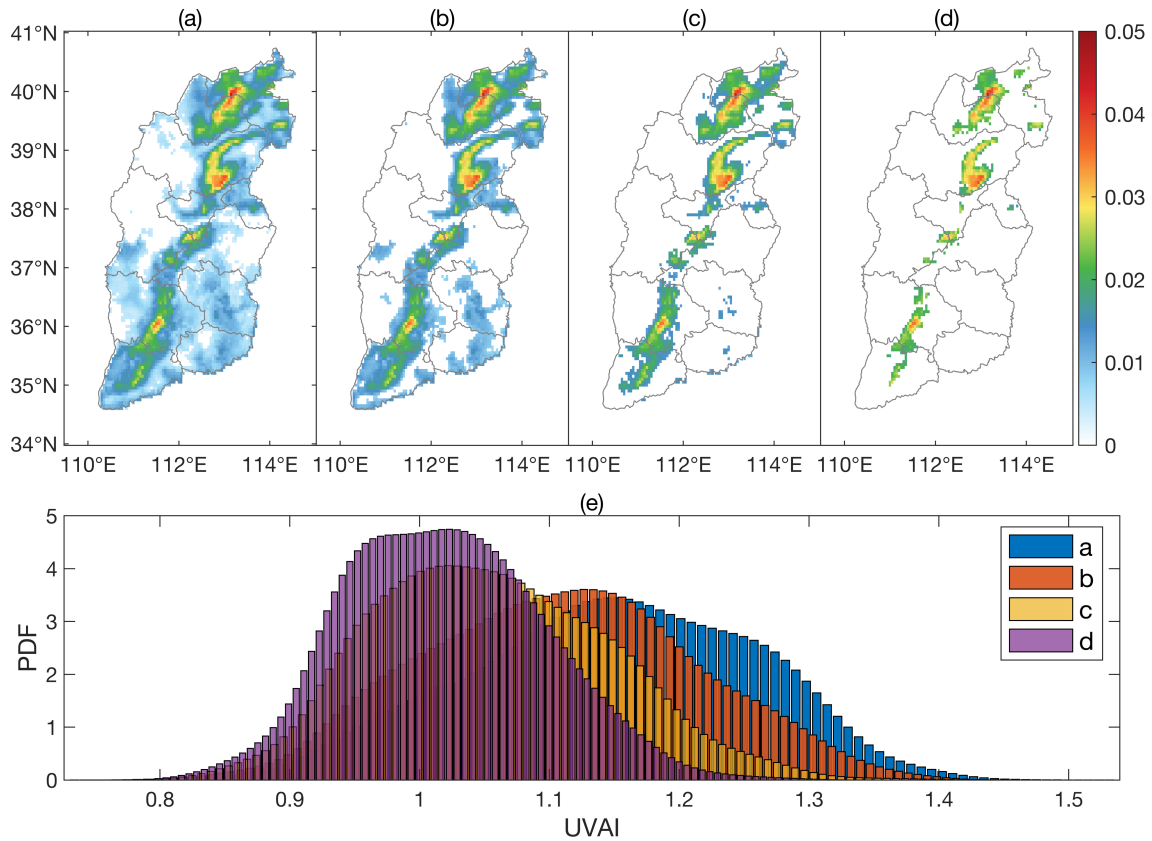
383



384

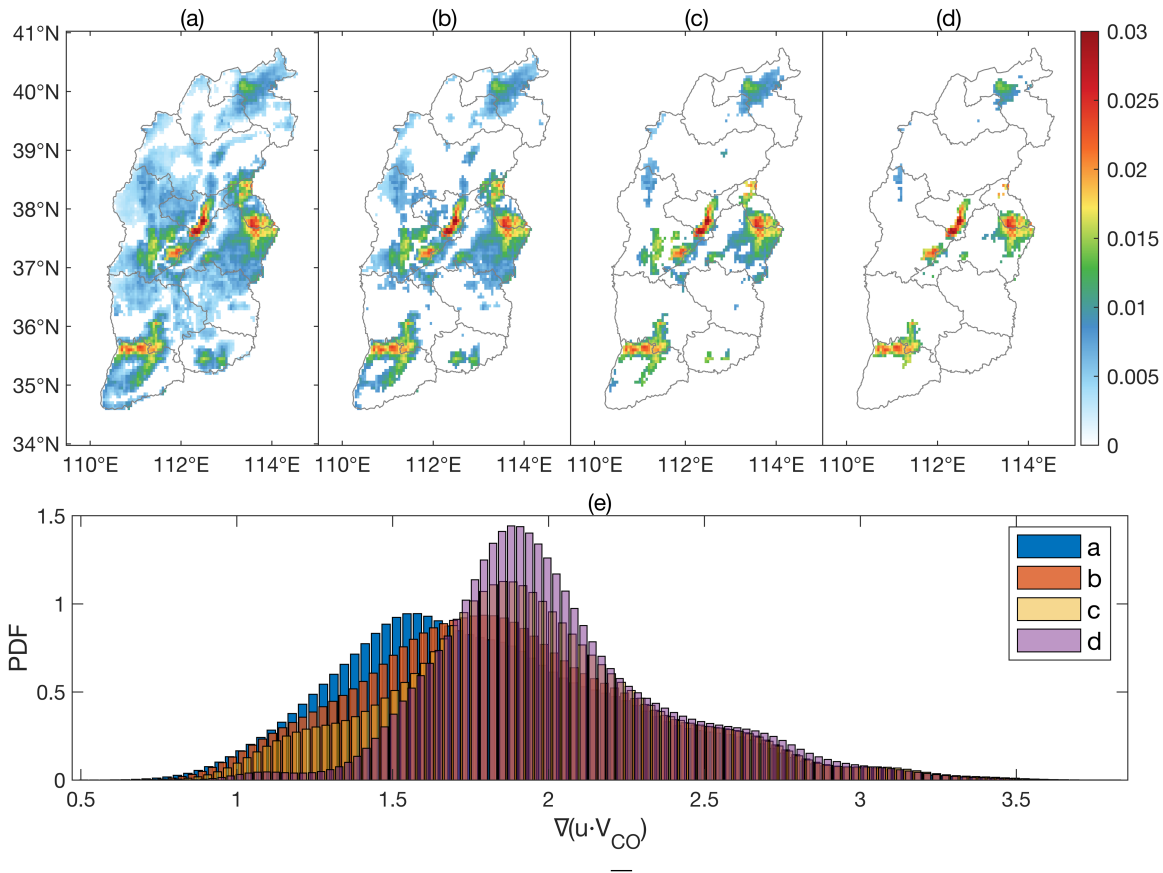
385 **Figure 7:** Four different cutoffs of EOF1 are used to set the domains. The maps in (a-d) are plots
386 of EOF1/Emissions where the cutoffs are given as (a) EOF1 >0.005, (b) EOF1 >0.01, (c)
387 EOF1 >0.015, (d) EOF1 >0.02. (e) Histograms of the emissions over the domains given
388 respectively in a-d.

389



390

391 **Figure 8:** Four different cutoffs of EOF2 are used to set the domains. The maps in (a-d) are plots
392 of EOF2/UVAI where the cutoffs are given as (a) EOF2 >0.005, (b) EOF2 >0.01,
393 EOF2 >0.015, (d) EOF2 >0.02. (e) Histograms of the UVAI over the domains given respectively
394 in a-d.



395

396 **Figure 9:** Four different cutoffs of EOF3 are used to set the domains. The maps in (a-d) are plots
 397 of EOF1/CO-transport where the cutoffs are given as (a) EOF3 > 0.005, (b) EOF3 > 0.01, (c)
 398 EOF3 > 0.015, (d) EOF3 > 0.02. (e) Histograms of the CO-transport over the domains given
 399 respectively in a-d.

400 3.3 Application of α_1 to Analyze Different Combustion Technologies

401 A significant finding is observed when the value of α_1 is analyzed more closely on a
 402 pixel-by-pixel level and compared with underlying CEMS combustion source type. This analysis
 403 is motivated by the fact that NO_x is produced during high temperature combustion of air, with
 404 three different major parts contributing to the overall amount of NO_x produced: thermal NO_x
 405 formation, fuel NO_x formation and chemical NO_x formation (Le Bris et al., 2007; Schwerdt,
 406 2006). This work demonstrates clearly that the values of α_1 are significantly related to the
 407 underlying thermodynamic conditions occurring at the time of combustion, allowing for many
 408 future applications of the results herein to better understand and monitor such plants around the
 409 world.

410 Thermal NO_x formation describes the process when N_2 in the air reacts with O_2 in the air
 411 at high temperatures (Le Bris et al., 2007), with NO_2 forming preferentially at temperatures
 412 between 800°C and 1200°C and NO forming preferentially at temperatures above 1200°C.
 413 Thermal NO_x usually dominates the overall NO_x emissions when the temperature is over
 414 1100°C, and reaches a maximum contribution when the temperature is over 1600 °C. There is
 415 additional NO_x produced due to free nitrogen in the fuel itself. Finally, chemical decay may

416 occur when there are mixed organo-nitrides, resulting in the prompt NO_x formation. Therefore, a
417 deeper understanding of the overall and oxygen partial pressures and temperature in the
418 combustion chamber are all important for NO_x formation. First, as the temperature increases, the
419 amount of NO produced will increase along with NO₂. When the temperature exceeds 1200°C,
420 NO will continue to increase while NO₂ will decrease. Furthermore, when the pressure increases,
421 the yield of NO₂ will also decrease and NO will increase (Aho et al., 1995; Turns, 1995).

422 In addition, in-situ processes also impact the value of α_1 since there is a rapid adjustment
423 after emitted from a combustion stack into the atmosphere, before the parcel comes to
424 thermodynamic equilibrium (Cohen et al., 2018; Wang et al., 2020). Figure 10 shows the results
425 of α_1 calculated based on CEMS in this study, and it can be seen that the values are highest in the
426 hottest months without maximum UV (July and August) and are lowest in the coldest months
427 with the minimum UV (November, December, and January), with both factors moderating the
428 combustion values during the atmospheric in-situ processing time. This is especially important in
429 the case of hotter power sources, since they will contain more buoyancy, and rise to a higher
430 height, making them more likely to be in contact with air which is more exposed to UV and also
431 generally colder than the surface. Overall, the value of α_1 seems to rely on both the temperature
432 under which the initial NO_x was generated, as well as any rapid processes taking place once it is
433 emitted into the atmosphere (including chemistry and vertical lofting).

434 A deeper look at the various different CEMS plant sources reveals that the internal
435 combustion processes are extremely important in terms of the overall value of α_1 . Production of
436 cement is a major source of NO_x in Shanxi, with the major technology being dry process rotary
437 kiln technology. Given that the temperature of the main burner of cement rotary kilns are higher
438 than 1400°C, with some peaking as high as 1800 °C to 2000 °C (Akgun, 2003; Wu et al., 2020),
439 it is expected that there will be a large amount of thermodynamic NO_x generation. As observed
440 at the cement CEMS sites, the computed α_1 has a value always within or above the error range of
441 the values computed at powerplants, including some of the individually highest values, as show
442 in figure 10b.

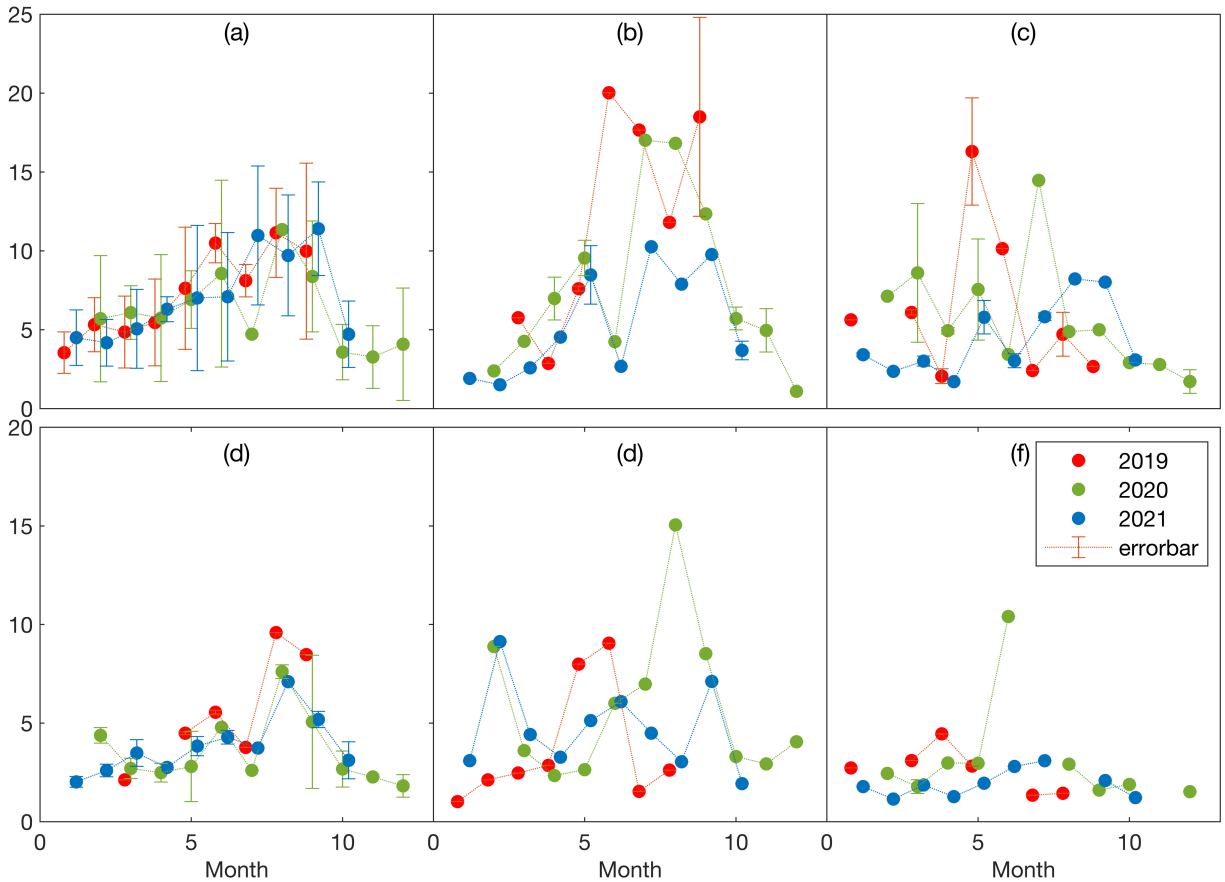
443 Steel and iron are produced through a set of different processes, involving combustion at
444 a range of different temperatures. The steps involved in the blast furnaces as well as some other
445 processes, require a high flame temperature, in the range from 1350 °C to 2000 °C. There are
446 further processes occurring that require a relatively lower temperature, such as in the sinter bed
447 stage, where the highest temperature is only about 1300 °C (Zhou et al., 2018). Therefore, while
448 in general the values are relatively high, and are usually found within the ranges of power plants,
449 there are some individual values of α_1 computed which are slightly outside the range of the
450 powerplant α_1 values, on both the high and low sides, as observed in figure 10c.

451 The maximum temperature of the combustion chamber of thermal power plants can reach
452 2000°C. In fact, many such plants are constantly finding ways to increase the combustion
453 efficiency of power plants, so that they can be more energy efficient and produce as much energy
454 per ton of CO₂ emitted, which in turn increases the combustion temperature. As observed in
455 Figure10a, α_1 is relatively high at these sites, consistent with thermal production.

456 Industrial boilers use a similar technology as power plants, but tend to be smaller and run
457 at a lower temperature range and efficiency. This is because their use is to produce hot water and
458 steam for direct residential and industrial use, not high-pressure steam to run turbines. In general,
459 these boilers have a much smaller overall capacity (as small as one tenth the total power output)

460 and therefore without access to CEMS, may not be otherwise be detectable. However, analyzing
461 the values of α_1 over these sites corresponding to the CEMS map, as displayed in figure 10f, the
462 results are found to have a value of α_1 that is lower than power plants in general, although also
463 smooth and consistent over different months of the year. That these sites produce NO_x with a far
464 greater amount of NO_2 than the above cases is as expected.

465 Coke and aluminum oxide are both produced using a different technique from the other
466 combustion sources, specifically focusing on creating high temperature, oven-like conditions to
467 bake/roast their products. The average temperature of the coke oven charring chamber and
468 aluminum oxide roasting furnace are around 1000°C (Neto et al., 2021; Abyzov, 2019), with the
469 material temperature continuously held in that temperature for a long period of time, e.g., one
470 day. At the same time, the oxygen content is low. Aluminum is also smelted in an oven-like
471 condition. In net, there is far less thermal NO and more thermal NO_2 . Correspondingly, the
472 values of α_1 are relatively lower, as detailed in figure 10d and figure 10e. Furthermore, due to
473 very different technologies and input materials used, the results are also observed to have a far
474 greater variance both intra-annually and inter-annually than the other sources.
475



476

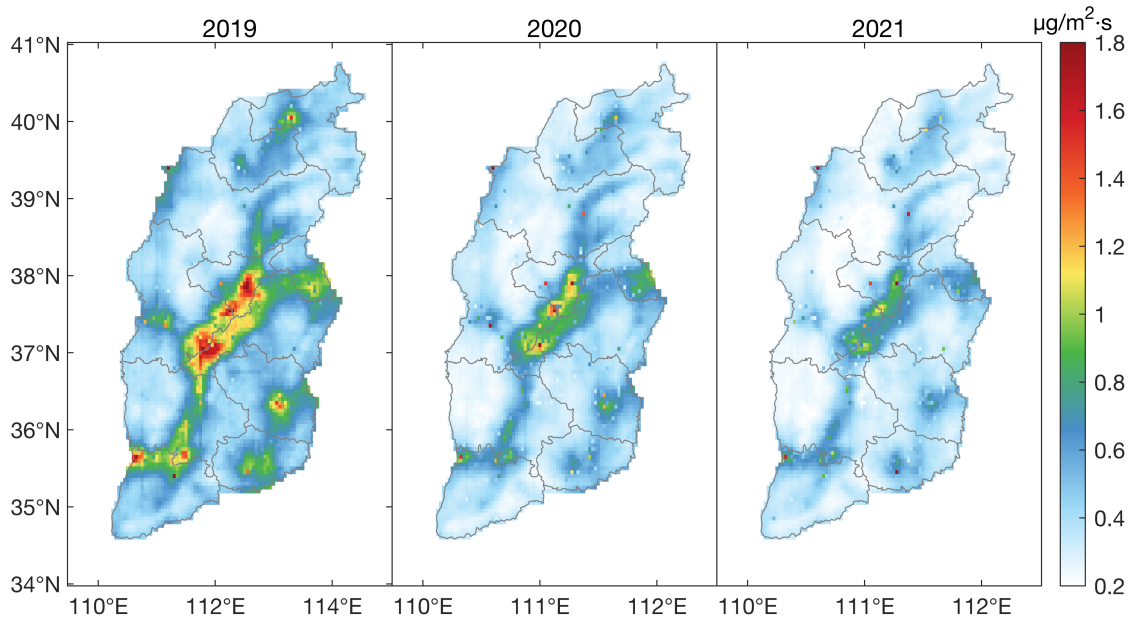
477 **Figure 10:** Monthly α_1 calculated based on CEMS for different factories of 2019, 2020 and
 478 2021, respectively: (top-left) Power plants; (top-center) Cement factories; (top-right) Steel and
 479 iron factories; (bottom-left) Coke ovens; (bottom-center) Aluminum oxide factories; (bottom-
 480 right) Boilers.

481 3.4 Yearly Changes of CEMS Calculated Emissions

482 Figure 11 shows the calculated results of CEMS emissions from February to September
 483 in 2019, 2020, and 2021, have average emission intensities of 0.52 ± 0.31 , 0.42 ± 0.21 , and
 484 $0.37 \pm 0.18 \mu\text{g}/\text{m}^2 \cdot \text{s}$, respectively. The emission intensity in 2020 is much less than that in 2019,
 485 with a continued albeit smaller decrease from 2020 to 2021, coupled with a continued reduction
 486 in the day-to-day variability. This overall change is because of the more stagnant production and
 487 other related economic activities during the control of COVID-19 in 2020, as well as a strong
 488 overlap with long-term air pollution control measurements, such as the ultra-low strategy on steel
 489 and iron, and cement factories, which were put in place long before COVID-19 and expected to
 490 successfully achieve a low emissions level by the end of 2021.

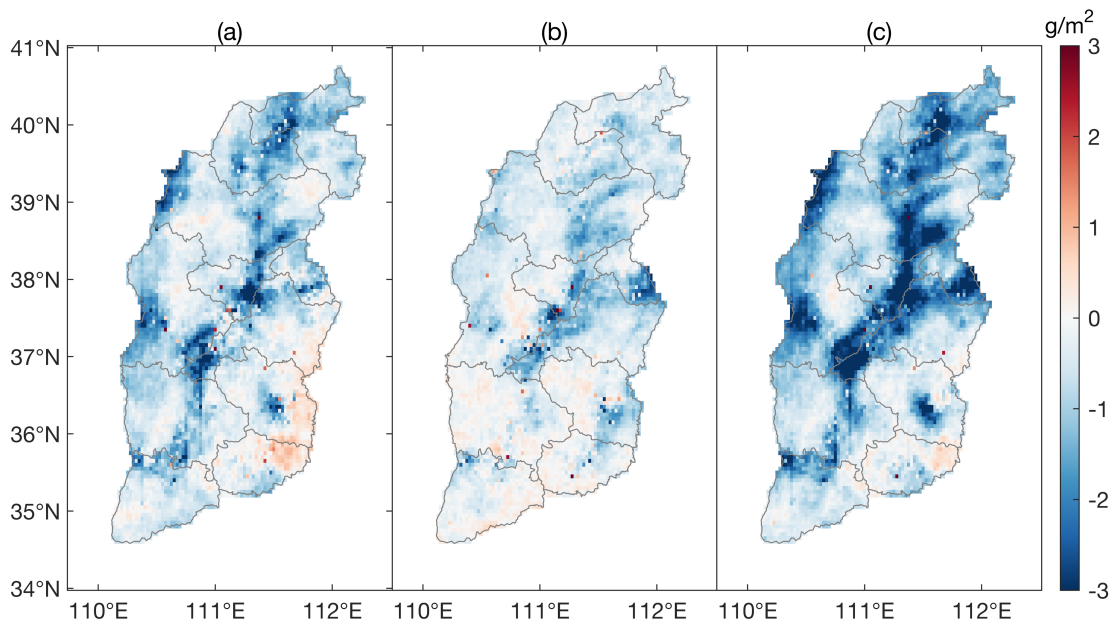
491 There are also some differences in hotspot areas. By comparing with the distribution map
 492 of industrial parks, CEMS enterprises, and district and county distribution map in Shanxi, it can
 493 be found that almost all of the individual grids with an increase in emissions in 2020 occur in
 494 areas outside industrial and city center areas. In specific, the most obvious increase is observed

495 in the rural boarder area between southeastern Shanxi and Henan Province, including parts of
496 Lingchuan, Gaoping, Zezhou, and Qinshui Counties and areas outside of the urban area of
497 Jincheng City. Huguan, Pinshun, Licheng Counties in Changzhi City, Zuoquan and Heshun
498 Counties in Jinzhong City adjacent to Handan City in Hebei Province also have a large increase.
499 While a part of this increase may be due to transport from surrounding areas of adjacent
500 provinces, based on the results of Figure 9 this is not very significant. Therefore, the most likely
501 explanation is that when COVID-19 first occurred, people stayed in their rural hometowns and
502 continued to cook and heat their homes, as compared to moving to the urban areas for
503 employment. Similarly, the reduction in emissions in urban and industrial areas is mainly due to
504 the reduction in industrial production and of shrinking transport flow in cities. Part of the
505 increase in 2021 relative to 2020 is observed in grids where there is an observed resumption of
506 previously shutdown industries and the widespread resumption of road traffic. Jincheng,
507 Changzhi, and Jinzhong Cities increased obviously in 2020 but then saturated and did not show a
508 significant increase during 2021. The southwest corner of Shanxi, Linfen, Yuncheng Cities and
509 other places increased more in 2021, perhaps related to increased production and subsequent
510 pollution transport from Henan and Shaanxi Provinces, as consistent with Figure 12b. From the
511 two-year change (figure 12c), the overall emissions of NO_x demonstrate a very obvious
512 weakening, especially in Datong, the Xinding basin, and the Taiyuan basin, which includes the
513 largest city centers and industrial belts in the province.
514



515

516 **Figure 11:** Daily average NO_x emissions based on CEMS in different years: (a) Climatological
 517 mean emissions of 2019 February to September; (b) Climatological mean of 2020 February to
 518 September; (c) Climatological mean of 2021 February to September.



519

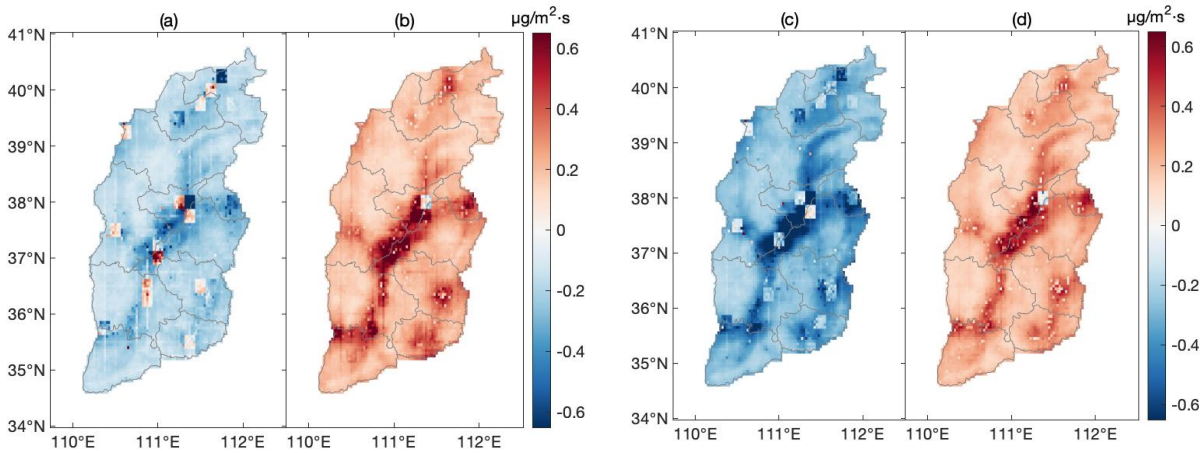
520 **Figure 12:** The difference between NO_x emissions over Shanxi calculate based on CEMS in
 521 different year: (a) Daily average mean NO_x Emission of 2020 minus that of 2019; (b) Daily

522 average mean NO_x Emission of 2021 minus that of 2020; (c) Daily average mean NO_x Emission
523 of 2021 minus that of 2019.

524 3.5 Differences between Computed Emissions and a Prior Emissions Inventories

525 Three different sets of optimized emissions are calculated using MFIEF forced by
526 different a prior emissions inventories. The differences between the MFIEF emissions using
527 CEMS, MEIC050 and Merged014 are displayed in Figure 13. In general, MFIEF based on
528 MEIC050 is larger than MFIEF based on CEMS, with the major exception occurring in pixels
529 containing major polluting sources such as iron, steel, and power plants inside Taiyuan City, the
530 thermal power plants in Datong, and industrial regions in Lvliang, Jinzhong, and other cities. The
531 observed gap between the results in 2020 is even larger than in 2019, even though the overall
532 emissions in 2020 are smaller than in 2019. These differences may be due to slightly mis-
533 positioned hotspots in the existing inventory. These extreme values tend to lead to either biased
534 values of α_1 and α_2 , or values which are physically impossible and therefore are discarded.
535 Furthermore, the difference between urban centers in Changzhi, Jincheng, Linfen, and Lvliang
536 may be due to the fact that CEMS better captures and detects residential sources and other
537 sources of moderate emissions, as compared with MEIC.

538 Next, the results of MFIEF based on Merged014 are usually smaller than the results of
539 MFIEF based on CEMS, with the exception of iron, steel, and power plants inside Taiyuan and
540 some other large sources where CEMS factories are located. This is because many of the grids in
541 Merged014 are so small, that when added to the original CEMS inventory, the PDF of the best fit
542 values of α_1 were shifted smaller. At the same time the values of α_2 were shifted longer. In
543 tandem with these, the transport term α_3 was shifted to include larger absolute values of
544 distance, which therefore caused the final calculation to be smaller overall. Similarly, some of
545 these shifts were so large as to make the values of α_1 and α_2 physically impossible, and
546 therefore be discarded. A similar set of shifts is observed as well when transitioning from
547 MEIC050 to MEIC014, and more so from MEIC014 to MEIC. Although mathematically correct,
548 since these shifts are not as reasonable from a physical or chemical perspective, these choices are
549 considered to be less optimal than purely relying on CEMS for the a priori value.
550



551

552 **Figure 13:** Computed grid-by-grid annual differences based on different a priori emissions
 553 inventories: (a) MFIEF CEMS minus MFIEF MEIC015 (February - September 2019), (b)
 554 MFIEF CEMS minus MFIEF Merged014 (February - September 2019), (c) MFIEF CEMS
 555 minus MFIEF MEIC015 (February - September 2020), (d) MFIEF CEMS minus MFIEF
 556 Merged014 (February - September 2020).

557 4 Conclusions

558 MFIEF computed emissions based on daily measurements from TROPOMI and a priori
 559 daily emissions from CEMS very successfully inverts daily NO_x emissions over a multi-year
 560 period in a rapidly developing part of China. First, the emissions computed match well with
 561 known urban, suburban, and industrial locations. Second, the best fit values for thermodynamics
 562 (α_1) and first order chemical decay (α_2) are both physically realistic, while the best fit term for
 563 transport (α_3) is reasonable based on the mountainous terrain and extensive basin-based
 564 geography of the province. Third, the computed emissions with respect to geography, month of
 565 the year, and years before and after COVID-19 are consistent with other findings from the
 566 community. Fourth, the uncertainty is observed to be lower than the day-to-day variability,
 567 showing that the results are statistically significant at the day-to-day level.

568 The MFIEF emissions computed using different a priori emissions datasets yield
 569 significant differences, which are not consistent with CEMS measurements or on-the-ground
 570 knowledge. The use of MEIC as an a priori severely underestimates lower and newer sources,
 571 while overestimating sources in the provincial capital of Taiyuan and its enormous steel iron
 572 plant. The MFIEF emissions computed using the mixed MEIC with CEMS a priori weights too
 573 many low values from MEIC in the suburban and rural areas, leading to physically unreasonable
 574 and very low/high biased values of α_1/α_2 values. The computed uncertainties in all of these other
 575 cases are also observed to be larger than in the base CEMS case, further indicating that these
 576 other cases are not as successful. Since MEIC is constructed similarly to EDGAR and other
 577 bottom-up emissions databases, it is possible that similar biases and results may be found in
 578 other parts of the world with respect to the geospatial biases of NO_x emissions.

579 The results of a variance maximization analysis of the daily TROPOMI NO_2 columns
 580 reveal three geospatial patterns that drive the NO_2 fields. This work's computed MFIEF
 581 emissions with CEMS is attributed as responsible for pattern 1, measured UV from TROPOMI
 582 (which induces photochemistry) is attributed as responsible for pattern 2, while transport

583 (computed from reanalysis wind and TROPOMI measured CO columns) is attributed as
584 responsible for pattern 3. The authors recommend that subsequent emissions analysis work from
585 both model-based and remotely-sensed based perspectives should follow a similar procedure, to
586 ensure that the results do not only match on average, but also make sense based on the observed
587 spatial and temporal gradients of the observed remotely sensed fields.

588 Finally, it is observed that the calculated values of α_1 are very highly correlated with the
589 thermodynamic conditions of underlying large combustion sources, offering consistency that the
590 term α_1 is a strong function of the combustion conditions under which NO_x is generated. At
591 locations which have CEMS power plants α_1 is consistently high. At locations that have CEMS
592 steel/iron and cement plants, α_1 is very high, but also has less consistency. Locations that have
593 CEMS aluminum plants generally are low, but have a few individual high values of α_1 .
594 Locations that have CEMS Coke plants always have a low value of α_1 , while locations with
595 boilers consistently have the lowest α_1 . There is a slight offset based on the atmospheric
596 temperature and UV radiation, with both colder and lower radiation months having α_1 slightly
597 negatively offset and months with hotter and higher radiation conditions having α_1 slightly
598 positively offset. This is consistent across all plant types, but especially so for the hottest types
599 (Iron/Steel, Cement, and Electricity), which are most likely to rise to a higher elevation and
600 therefore be more impacted by the surrounding atmospheric conditions. These findings allow an
601 extension of this approach to monitoring, identifying, or mode deeply understanding dedicated
602 moderate to large emissions sources in regions which may not have surface-based monitoring.

603 The procedure introduced here offers a next step advance in terms of computing
604 emissions from a top-down perspective. The authors urge the community to adopt and use these
605 new results, while also using them to improve their own bottom-up inventories and attribution
606 techniques. This work would be greatly improved by reduction in remotely sensed measurement
607 errors/uncertainties, increased use of and access to surface CEMS and other flux measurements,
608 and improved a priori emissions databases. One of the easiest ways for improvement would be
609 for bottom-up inventories to adopt the day-to-day and other forms of variation, as well as
610 quantitative error analyses. The ability to identify large and moderately large plants and
611 industrial sources could be used to identify and quantify sources from many parts of the Global
612 South where ground-based measurements may not be readily available. Finally, such objective
613 approaches will hopefully be improved, allowing for more precision and predictability, so that
614 emissions and environmental regulators can have more quantitative support to focus their efforts.

615 **Acknowledgments**

616 The authors would like to thank the continuous emissions monitoring systems (CEMS)
617 for the provision of their in situ data. This work thanks the PIs of the TROPOMI, ERA-5, MEIC
618 products for making their data available. The study was supported by the National Natural
619 Science Foundation of China (42075147), the Shanxi Province Major Science and Technique
620 Program (202101090301013), and the Shanxi Province Postgraduate Education Innovation
621 Program (2021Y035). The authors declare that they have no conflict of interest.

622 **Author contributions**

623 Conceptualization: Jason Blake Cohen; Formal Analysis: Xiaolu Li, Jason Blake Cohen;
624 Funding Acquisition: Jason Blake Cohen, Kai Qin; Investigation: Xiaolu Li, Jason Blake Cohen,
625 Kai Qin and Hong Geng; Methodology: Xiaolu Li, Jason Blake Cohen, Kai Qin; Resources:
626 Hong Geng, Liling Wu, Xiaohui Wu, Chengli Yang, Rui Zhang, and Liqin Zhang Software:
627 Xiaolu Li; Supervision: Jason Blake Cohen, Kai Qin, Hong Geng; Validation: Xiaolu Li, Jason
628 Blake Cohen; Visualization: Xiaolu Li; Writing – original draft: Xiaolu Li, Jason Blake Cohen;
629 Writing – review & editing: Xiaolu Li, Jason Blake Cohen, Kai Qin, Hong Geng.

630 **Data Availability Statement**

631 The satellite NO₂ datasets used in this study are available at
632 <https://disc.gsfc.nasa.gov/datasets>. The ERA-5 reanalysis product is available at
633 <https://doi.org/10.24381/cds.bd0915c6>. The CEMS online data is available at
634 <https://sthjt.shanxi.gov.cn/wryjg>. The MEIC product can be accessed from
635 <https://doi.org/10.6084/m9.figshare.c.5214920.v2> (Zheng et al., 2021). All of the data, including
636 CEMS and underlying figures are available for download at
637 <https://figshare.com/s/22782c33cbc4e61afd25>

638 **References**

- 639 Abyzov, A. (2019). Aluminum oxide and alumina ceramics (review). Part 1. Properties of Al₂O₃
640 and commercial production of dispersed Al₂O₃. *Refractories and industrial ceramics*,
641 *60*(1), 24-32. <http://doi.org/10.1007/s11148-019-00304-2>
- 642 Aho, M. J., Paakkinen, K. M., Pirkonen, P. M., Kilpinen, P., & Hupa, M. (1995). The effects of
643 pressure, oxygen partial pressure, and temperature on the formation of N₂O, NO, and
644 NO₂ from pulverized coal. *Combustion and Flame*, *102*(3), 387-400.
645 [https://doi.org/10.1016/0010-2180\(95\)00019-3](https://doi.org/10.1016/0010-2180(95)00019-3)
- 646 Akgun, F. (2003). Investigaton of energy saving and NO_x reduction possibilities in a rotary
647 cement kiln. *International journal of energy research*, *27*(4), 455-465.
648 <https://doi.org/10.1002/er.888>
- 649 Beirle, S., Boersma, K. F., Platt, U., Lawrence, M. G., & Wagner, T. (2011). Megacity
650 Emissions and Lifetimes of Nitrogen Oxides Probed from Space. *Science*, *333*(6050),
651 1737-1739. <https://doi.org/10.1126/science.1207824>
- 652 Beirle, S., Borger, C., Dorner, S., Li, A., Hu, Z. K., Liu, F., et al. (2019). Pinpointing nitrogen
653 oxide emissions from space. *Science Advances*, *5*(11).
654 <https://www.science.org/doi/10.1126/sciadv.aax9800>
- 655 Björnsson, H., & Venegas, S. (1997). A manual for EOF and SVD analyses of climatic data.
656 *CCGCR Report*, *97*(1), 112-134. McGill University.

- 657 Bond, T. C. (2004). A technology-based global inventory of black and organic carbon emissions
658 from combustion. *Journal of Geophysical Research*, 109(D14).
659 <https://doi.org/10.1029/2003JD003697>
- 660 Chen, Y. H., & Prinn, R. G. (2006). Estimation of atmospheric methane emissions between 1996
661 and 2001 using a three-dimensional global chemical transport model. *Journal of*
662 *Geophysical Research: Atmospheres*, 111(D10). <https://doi.org/10.1029/2005JD006058>
- 663 Cohen, J. B. (2014). Quantifying the occurrence and magnitude of the Southeast Asian fire
664 climatology. *Environmental Research Letters*, 9(11). [https://doi.org/10.1088/1748-](https://doi.org/10.1088/1748-9326/9/11/114018)
665 [9326/9/11/114018](https://doi.org/10.1088/1748-9326/9/11/114018)
- 666 Cohen, J. B., Lecoer, E., & Hui Loong Ng, D. (2017). Decadal-scale relationship between
667 measurements of aerosols, land-use change, and fire over Southeast Asia. *Atmospheric*
668 *Chemistry and Physics*, 17(1), 721-743. <https://doi.org/10.5194/acp-17-721-2017>
- 669 Cohen, J. B., Ng, D. H. L., Lim, A. W. L., & Chua, X. R. (2018). Vertical distribution of
670 aerosols over the Maritime Continent during El Nino. *Atmospheric Chemistry and*
671 *Physics*, 18(10), 7095-7108. <https://doi.org/18/7095/2018/acp-18-7095-2018>
- 672 Cohen, J. B., & Wang, C. (2014). Estimating global black carbon emissions using a top-down
673 Kalman Filter approach. *Journal of Geophysical Research-Atmospheres*, 119(1), 307-
674 323. <https://doi.org/10.1002/2013jd019912>
- 675 Crippa, M., Guizzardi, D., Muntean, M., Schaaf, E., Dentener, F., van Aardenne, J. A., et al.
676 (2018). Gridded emissions of air pollutants for the period 1970–2012 within EDGAR
677 v4.3.2. *Earth System Science Data*, 10(4), 1987-2013. [https://doi.org/10.5194/essd-10-](https://doi.org/10.5194/essd-10-1987-2018)
678 [1987-2018](https://doi.org/10.5194/essd-10-1987-2018)
- 679 Eskes, H., Geffen, J. v., Boersma, F., Eichmann, K.-U., Apituley, A., Pedernana, M., et al.
680 (2021). *Sentinel-5 precursor/TROPOMI Level 2 Product User Manual Nitrogen dioxide*.
681 Royal Netherlands Meteorological Institute.
- 682 Fioletov, V., McLinden, C. A., Griffin, D., Krotkov, N., Liu, F., & Eskes, H. (2022). Quantifying
683 urban, industrial, and background changes in NO₂ during the COVID-19 lockdown
684 period based on TROPOMI satellite observations. *Atmospheric Chemistry and Physics*,
685 22(6), 4201-4236. <https://doi.org/10.5194/acp-22-4201-2022>
- 686 Geng, G., Xiao, Q., Zheng, Y., Tong, D., Zhang, Y., Zhang, X., et al. (2019). Impact of China's
687 air pollution prevention and control action plan on PM_{2.5} chemical composition over

- 688 eastern China. *Science China Earth Sciences*, 62(12), 1872-1884.
689 <https://doi.org/10.1007/s11430-018-9353-x>
- 690 Goldberg, D. L., Lu, Z., Streets, D. G., de Foy, B., Griffin, D., McLinden, C. A., et al. (2019).
691 Enhanced capabilities of TROPOMI NO₂: estimating NO_x from North American Cities
692 and power plants. *Environmental Science & Technology*, 53(21), 12594-12601.
693 <https://doi.org/10.1021/acs.est.9b04488>
- 694 Griffin, D., McLinden, C. A., Boersma, F., Bourassa, A., Dammers, E., Degenstein, D., et al.
695 (2019). High resolution mapping of nitrogen dioxide with TROPOMI: First results and
696 validation over the Canadian oil sands. *Geophysical Research Letters*, 46(2), 1049-1060.
697 <https://doi.org/10.1029/2018GL081095>
- 698 Hoesly, R. M., Smith, S. J., Feng, L., Klimont, Z., Janssens-Maenhout, G., Pitkanen, T., et al.
699 (2018). Historical (1750-2014) anthropogenic emissions of reactive gases and aerosols
700 from the Community Emissions Data System (CEDS). *Geoscientific Model Development*,
701 11(1), 369-408. <https://doi.org/10.5194/gmd-11-369-2018>
- 702 Hu, Y., Zang, Z., Chen, D., Ma, X., Liang, Y., You, W., et al. (2022). Optimization and
703 evaluation of SO₂ emissions based on WRF-Chem and 3DVAR data assimilation, *Remote*
704 *Sensing*, 14(1), 220. <https://doi.org/10.3390/rs14010220>
- 705 Jacob, D. J., Logan, J. A., Gardner, G. M., Yevich, R. M., Spivakovsky, C. M., Wofsy, S. C., et
706 al. (1993). Factors regulating ozone over the United States and its export to the global
707 atmosphere. *Journal of Geophysical Research: Atmospheres*, 98(D8), 14817-14826.
708 <https://doi.org/10.1029/98JD01224>
- 709 Jiang, X., Li, G., & Fu, W. (2021). Government environmental governance, structural adjustment
710 and air quality: A quasi-natural experiment based on the Three-year Action Plan to Win
711 the Blue Sky Defense War. *Journal of Environmental Management*, 277, 111470.
712 <https://doi.org/10.1029/2018GL081095>
- 713 Karplus, V. J., Zhang, S., & Almond, D. (2018). Quantifying coal power plant responses to
714 tighter SO₂ emissions standards in China. *Proc Natl Acad Sci U S A*, 115(27), 7004-
715 7009. <https://doi.org/10.1073/pnas.1800605115>
- 716 Kong, H., Lin, J., Zhang, R., Liu, M., Weng, H., Ni, R., et al. (2019). High-resolution
717 (0.05° × 0.05°) NO_x emissions in the Yangtze River Delta inferred from OMI.

- 718 *Atmospheric Chemistry and Physics*, 19(20), 12835-12856.
719 <https://doi.org/10.5194/acp19-12835-2019>
- 720 Lange, K., Richter, A., & Burrows, J. P. (2022). Variability of nitrogen oxide emission fluxes
721 and lifetimes estimated from Sentinel-5P TROPOMI observations. *Atmospheric*
722 *Chemistry and Physics*, 22(4), 2745-2767. <https://doi.org/10.5194/acp-22-2745-2022>
- 723 Le Bris, T., Cadavid, F., Caillat, S., Pietrzyk, S., Blondin, J., & Baudoin, B. (2007). Coal
724 combustion modelling of large power plant, for NO_x abatement. *Fuel*, 86(14), 2213-2220.
725 <https://doi.org/10.1016/j.fuel.2007.05.054>
- 726 Li, H., Zhang, J., Wen, B., Huang, S., Gao, S., Li, H., et al. (2022). Spatial-Temporal
727 Distribution and Variation of NO₂ and Its Sources and Chemical Sinks in Shanxi
728 Province, China. *Atmosphere*, 13(7), 1096. <https://doi.org/10.3390/atmos13071096>
- 729 Lin, C., Cohen, J. B., Wang, S., & Lan, R. (2020). Application of a combined standard deviation
730 and mean based approach to MOPITT CO column data, and resulting improved
731 representation of biomass burning and urban air pollution sources. *Remote Sensing of*
732 *Environment*, 241, 111720. <https://doi.org/10.1016/j.rse.2020.111720>
- 733 Liu, J., & Cohen, J. (2022). Quantifying the Missing Half of Daily NO_x Emissions over South,
734 Southeast and East Asia. <https://doi.org/10.21203/rs.3.rs-1613262/v1>
- 735 Mahowald, N. M., Baker, A. R., Bergametti, G., Brooks, N., Duce, R. A., Jickells, T. D., et al.
736 (2005). Atmospheric global dust cycle and iron inputs to the ocean. *Global*
737 *Biogeochemical Cycles*, 19(4). <https://doi.org/10.1029/2004gb002402>
- 738 Mijling, B., & van der A, R. J. (2012). Using daily satellite observations to estimate emissions of
739 short-lived air pollutants on a mesoscopic scale. *Journal of Geophysical Research:*
740 *Atmospheres*, 117(D17). <https://doi.org/10.1029/2012JD017817>.
- 741 Neto, G. F., Leite, M., Marcelino, T., Carneiro, L., Brito, K., & Brito, R. (2021). Optimizing the
742 coke oven process by adjusting the temperature of the combustion chambers. *Energy*,
743 217, 119419. <https://doi.org/10.1016/j.energy.2020.119419>
- 744 Qin, K., Shi, J., He, Q., Deng, W., Wang, S., Liu, J., & Cohen, J. B. (2022). New Model-Free
745 Daily Inversion of NO_x Emissions using TROPOMI (MCMFE-NO_x): Deducing a See-
746 Saw of Halved Well Regulated Sources and Doubled New Sources. *Earth and Space*
747 *Science Open Archive*, 26. <https://doi.org/10.1002/essoar.10512010.1>

- 748 Schreifels, J. J., Fu, Y. L., & Wilson, E. J. (2012). Sulfur dioxide control in China: policy
749 evolution during the 10th and 11th Five-year Plans and lessons for the future. *Energy*
750 *Policy*, 48, 779-789. <https://doi.org/10.1016/j.enpol.2012.06.015>
- 751 Schwerdt, C. (2006). *Modelling NO_x-formation in combustion processes*. Master Theses. Lund
752 University
- 753 Shanxi DEE. (2016, 2021). *Shanxi Province Ecology and Environment Status Bulletin*.
754 Department of Ecology and Environment of Shanxi Province.
755 <https://sthjt.shanxi.gov.cn/zwgk/hjgb/hjzkgb/index.shtml>
- 756 Singh, A., & Agrawal, M. (2008). Acid rain and its ecological consequences. *Journal of*
757 *Environmental Biology*, 29(1), 15-24.
- 758 Tang, L., Xue, X., Qu, J., Mi, Z., Bo, X., Chang, X., et al. (2020). Air pollution emissions from
759 Chinese power plants based on the continuous emission monitoring systems network. *Sci*
760 *Data*, 7(1), 325. <https://doi.org/10.1038/s41597-020-00665-1>
- 761 Tu, Q., Hase, F., Schneider, M., García, O., Blumenstock, T., Borsdorff, T., et al. (2022).
762 Quantification of CH₄ emissions from waste disposal sites near the city of Madrid using
763 ground- and space-based observations of COCCON, TROPOMI and IASI. *Atmospheric*
764 *Chemistry and Physics*, 22(1), 295-317. <https://doi.org/10.5194/acp-22-295-2022>
- 765 Tu, Q., Schneider, M., Hase, F., Khosrawi, F., Ertl, B., Necki, J., et al. (2022). Quantifying CH₄
766 emissions in hard coal mines from TROPOMI and IASI observations using the wind-
767 assigned anomaly method. *Atmospheric Chemistry and Physics*, 22(15), 9747-9765.
768 <https://doi.org/10.5194/acp-22-9747-2022>
- 769 Turns, S. R. (1995). Understanding NO_x formation in nonpremixed flames: Experiments and
770 modeling. *Progress in Energy and Combustion Science*, 21(5), 361-385.
771 [https://doi.org/10.1016/0360-1285\(94\)00006-9](https://doi.org/10.1016/0360-1285(94)00006-9)
- 772 Valin, L. C., Russell, A. R., & Cohen, R. C. (2013). Variations of OH radical in an urban plume
773 inferred from NO₂ column measurements. *Geophysical Research Letters*, 40(9), 1856-
774 1860. <https://doi.org/10.1002/grl.50267>
- 775 Veefkind, J. P., Aben, I., McMullan, K., Förster, H., de Vries, J., Otter, G., et al. (2012).
776 TROPOMI on the ESA Sentinel-5 Precursor: A GMES mission for global observations of
777 the atmospheric composition for climate, air quality and ozone layer applications. *Remote*
778 *Sensing of Environment*, 120, 70-83. <https://doi.org/10.1016/j.rse.2011.09.027>

- 779 Wang, H., Rasch, P. J., Easter, R. C., Singh, B., Zhang, R., Ma, P. L., et al. (2014). Using an
780 explicit emission tagging method in global modeling of source-receptor relationships for
781 black carbon in the Arctic: Variations, sources, and transport pathways. *Journal of*
782 *Geophysical Research: Atmospheres*, 119(22). <https://doi.org/10.1002/2014jd022297>
- 783 Wang, S., Cohen, J. B., Deng, W., Qin, K., & Guo, J. (2021). Using a New Top-Down
784 Constrained Emissions Inventory to Attribute the Previously Unknown Source of
785 Extreme Aerosol Loadings Observed Annually in the Monsoon Asia Free Troposphere.
786 *Earth's Future*, 9(7). <https://doi.org/10.1029/2021ef002167>
- 787 Wang, S., Cohen, J. B., Lin, C. Y., & Deng, W. Z. (2020). Constraining the relationships
788 between aerosol height, aerosol optical depth and total column trace gas measurements
789 using remote sensing and models. *Atmospheric Chemistry and Physics*, 20(23), 15401-
790 15426. <https://doi.org/10.5194/acp-20-15401-2020>
- 791 Wu, H., Cai, J., Ren, Q., Shi, C., Zhao, A., & Lyu, Q. (2020). A thermal and chemical fuel
792 pretreatment process for NO_x reduction from cement kiln. *Fuel Processing Technology*,
793 210, 106556. <https://doi.org/10.1016/j.fuproc.2020.106556>
- 794 Zavala, M., Herndon, S. C., Slott, R. S., Dunlea, E. J., Marr, L. C., Shorter, J. H., et al. (2006).
795 Characterization of on-road vehicle emissions in the Mexico City Metropolitan Area
796 using a mobile laboratory in chase and fleet average measurement modes during the
797 MCMA-2003 field campaign. *Atmospheric Chemistry and Physics*, 6(12), 5129-5142.
798 <https://doi.org/10.5194/acp-6-5129-2006>
- 799 Zhang, X., & Schreifels, J. (2011). Continuous emission monitoring systems at power plants in
800 China: Improving SO₂ emission measurement. *Energy Policy*, 39(11), 7432-7438.
801 <https://doi.org/10.1016/j.enpol.2011.09.011>
- 802 Zhang, Z., Zang, Z., Cheng, X., Lu, C., Huang, S., Hu, Y., et al. (2021). Development of three-
803 dimensional variational data assimilation method of aerosol for the CMAQ model: an
804 application for PM_{2.5} and PM₁₀ forecasts in the sichuan basin. *Earth and Space Science*,
805 8(5), e2020EA001614. <https://doi.org/10.1029/2020EA001614>
- 806 Zhao, Y., Nielsen, C. P., Lei, Y., McElroy, M. B., & Hao, J. (2011). Quantifying the
807 uncertainties of a bottom-up emission inventory of anthropogenic atmospheric pollutants
808 in China. *Atmospheric Chemistry and Physics*, 11(5), 2295-2308.
809 <https://doi.org/10.5194/acp-11-2295-2011>

- 810 Zheng, B., Zhang, Q., Geng, G., Chen, C., Shi, Q., Cui, M., et al. (2021). Changes in China's
811 anthropogenic emissions and air quality during the COVID-19 pandemic in 2020. *Earth*
812 *System Science Data*, 13(6), 2895-2907. <https://doi.org/10.5194/essd-13-2895-2021>
- 813 Zheng, B., Zhang, Q., Tong, D., Chen, C., Hong, C., Li, M., et al. (2017). Resolution dependence
814 of uncertainties in gridded emission inventories: a case study in Hebei, China.
815 *Atmospheric Chemistry and Physics*, 17(2), 921-933. [https://doi.org/10.5194/acp-17-921-](https://doi.org/10.5194/acp-17-921-2017)
816 [2017](https://doi.org/10.5194/acp-17-921-2017)
- 817 Zhou, H., Ma, P., Cheng, M., Zhou, M., & Li, Y. (2018). Effects of temperature and circulating
818 flue gas components on combustion and NO_x emissions characteristics of four types
819 quasi-particles in iron ore sintering process. *ISIJ International*, 58(9), 1650-1658.
820 <https://doi.org/10.2355/isijinternational.ISIJINT-2018-185>
- 821 Zhou, S., Davy, P. K., Wang, X., Cohen, J. B., Liang, J., Huang, M., et al. (2016). High time-
822 resolved elemental components in fine and coarse particles in the Pearl River Delta
823 region of Southern China: Dynamic variations and effects of meteorology. *The Science of*
824 *the total environment*, 572, 634-648. <https://doi.org/10.1016/j.scitotenv.2016.05.194>
- 825
- 826
- 827